On the metallicity gradients of the Galactic disk as revealed by LSS-GAC red clump stars

Yang Huang[1], Xiao-Wei Liu[1,2], Hua-Wei Zhang[1,2], Hai-Bo Yuan[2], Mao-Sheng Xiang[1], Bing-Qiu Chen[2], Juan-Juan Ren[1], Ning-Chen Sun[1], Chun Wang[1], Yong Zhang[3], Yong-Hui Hou[3], Yue-Fei Wang[3] and Ming Yang[4]

[1] Department of Astronomy, Peking University, Beijing 100871, China; *yanghuang@pku.edu.cn; x.liu@pku.edu.cn; zhanghw@pku.edu.cn*
[2] Kavli Institute for Astronomy and Astrophysics, Peking University, Beijing 100871, China
[3] Nanjing Institute of Astronomical Optics & Technology, National Astronomical Observatories, Chinese Academy of Sciences, Nanjing 210042, China
[4] Key Laboratory of Optical Astronomy, National Astronomical Observatories, Chinese Academy of Sciences, Beijing 100012, China

Abstract Using a sample of over 70 000 red clump (RC) stars with 5%–10% distance accuracy selected from the LAMOST Spectroscopic Survey of the Galactic Anti-center (LSS-GAC), we study the radial and vertical gradients of the Galactic disk(s) mainly in the anti-center direction, covering a significant volume of the disk in the range of projected Galactocentric radius $7 \leq R_{\rm GC} \leq 14$ kpc and height from the Galactic midplane $0 \leq |Z| \leq 3$ kpc. Our analysis shows that both the radial and vertical metallicity gradients are negative across much of the volume of the disk that is probed, and they exhibit significant spatial variations. Near the solar circle ($7 \leq R_{\rm GC} \leq 11.5$ kpc), the radial gradient has a moderately steep, negative slope of -0.08 dex kpc^{-1} near the midplane ($|Z| < 0.1$ kpc), and the slope flattens with increasing $|Z|$. In the outer disk ($11.5 < R_{\rm GC} \leq 14$ kpc), the radial gradients have an essentially constant, much less steep slope of -0.01 dex kpc^{-1} at all heights above the plane, suggesting that the outer disk may have experienced an evolutionary path different from that of the inner disk. The vertical gradients are found to flatten largely with increasing $R_{\rm GC}$. However, the vertical gradient of the lower disk ($0 \leq |Z| \leq 1$ kpc) is found to flatten with $R_{\rm GC}$ quicker than that of the upper disk ($1 < |Z| \leq 3$ kpc). Our results should provide strong constraints on the theory of disk formation and evolution, as well as the underlying physical processes that shape the disk (e.g. gas flows, radial migration, and internal and external perturbations).

Key words: Galaxy: abundances — Galaxy: disk — Galaxy: evolution — Galaxy: formation — techniques: spectroscopic

1 INTRODUCTION

The distribution of metals in the disk of a galaxy is a consequence of a variety of complicated processes, including star formation and evolution, gas flows and stellar migration, non-axisymmetric

perturbations (e.g. by the central bar and spiral arms), and interactions and accretions. The stellar metallicity distribution in a disk galaxy, including our own Milky Way, typically exhibits a (negative) gradient in both the radial and vertical directions. Measurements of (radial and vertical) metallicity gradients are therefore of great importance for constraining the formation and evolution of galaxies, especially for the Milky Way.

The radial metallicity gradient of the Milky Way disk(s) has been measured using various tracers, including classical Cepheids (e.g. Andrievsky et al. 2002a,b,c, 2004; Luck et al. 2003, 2006, 2011; Kovtyukh et al. 2005; Yong et al. 2006; Lemasle et al. 2007, 2008; Pedicelli et al. 2009, 2010; Luck & Lambert 2011; Genovali et al. 2013, 2014; Martin et al. 2015), H II regions (e.g. Deharveng et al. 2000; Quireza et al. 2006; Rudolph et al. 2006; Balser et al. 2011), O/B-type stars (e.g. Smartt & Rolleston 1997; Gummersbach et al. 1998; Rolleston et al. 2000; Daflon & Cunha 2004; Daflon et al. 2009), open clusters (OCs; Friel et al. 2002, 2010; Chen et al. 2003; Yong et al. 2005, 2012; Carraro et al. 2007; Jacobson et al. 2008, 2009, 2011a,b; Magrini et al. 2009, 2010; Carrera & Pancino 2011; Frinchaboy et al. 2013) and planetary nebulae (PNe; Henry et al. 2004, 2010; Maciel et al. 2005; Stanghellini et al. 2006; Perinotto & Morbidelli 2006; Stanghellini & Haywood 2010). The above tracers are mainly close to the midplane and the sample sizes are generally limited to a few hundred targets. Recently, with the advent of large scale spectroscopic surveys of the Milky Way, radial gradients at different heights (Z) from the midplane and vertical gradients at different projected Galactocentric radii ($R_{\rm GC}$) have been measured with large numbers ($\sim$ tens of thousands) of field main-sequence/giant stars, such as main-sequence turnoff stars used by Cheng et al. (2012) from the SDSS/SEGUE (York et al. 2000; Yanny et al. 2009), both dwarf and giant stars used by Boeche et al. (2013, 2014) from the RAVE survey (Steinmetz et al. 2006), and red giants used by Hayden et al. (2014) from the SDSS-III/APOGEE (Allende Prieto et al. 2008; Ahn et al. 2014). Those tracers retain the chemical composition of the interstellar medium at the time of their birth. Hence, tracers of different ages probe metallicity gradients of the disk at different epochs. Near the solar circle ($7 < R_{\rm GC} < 10$ kpc), the measured radial gradients of the disk derived with different tracers range from -0.01 to -0.09 dex kpc^{-1} (e.g. Cheng et al. 2012; Lemasle et al. 2013) and the vertical gradients range from -0.07 to -0.30 dex kpc^{-1} (e.g. Katz et al. 2011; Chen et al. 2011; Kordopatis et al. 2011; Schlesinger et al. 2012, 2014). The negative radial gradients are generally explained with the so-called *inside-out* chemical evolution model (e.g, Larson 1976; Matteucci & Francois 1989; Chiappini et al. 1997, 2001; Hou et al. 2000; Prantzos & Boissier 2000; Mollá & Díaz 2005; Fu et al. 2009) in which the inner region of the disk is chemically enriched faster than the outer region.

However, there has been evidence that even close to the disk midplane, a simple linear relation may not be sufficient to describe the full variations of metallicity over the full range of $R_{\rm GC}$. Using classical Cepheids, several studies (e.g. Andrievsky et al. 2002b; Pedicelli et al. 2009, 2010; Luck & Lambert 2011; Genovali et al. 2013) have discovered that the radial gradient in the inner disk ($4 \le R_{\rm GC} \le 7$ kpc) is steeper than that near the solar circle. On the other hand, a flat, nearly zero radial gradient in the inner disk ($R_{\rm GC} \le 6$ kpc) has been found recently by Hayden et al. (2014) using APOGEE red giants. In the outer disk ($R_{\rm GC} > 10-12$ kpc), most studies based on OCs find that the radial gradients tend to be close to zero, and are flatter than those near the solar circle. Similar flat gradients in the outskirts of the disk are also reported by studies using other tracers, including H II regions (Vilchez & Esteban 1996), PNe (Costa et al. 2004) and classical Cepheids (Andrievsky et al. 2002c, 2004; Luck et al. 2003; Lemasle et al. 2008). However, it is still not clear that those observed flat gradients are real or simply due to the coarse sampling since almost all the aforementioned studies are based on samples containing only a few dozens of targets in the outer disk. More recently, more classical Cepheids have been found in the outer disk. The newly calculated radial gradient seems to have a value comparable to that near the solar circle, lending further evidence that the previously reported flat gradients in the outer disk may indeed be artifacts caused by the effects of poor sampling (e.g. Luck et al. 2011; Luck & Lambert 2011). From a theoretical point of

view, a flat radial gradient in the outer disk can be explained by the natural outcome of disk formation and evolution (e.g. Carraro et al. 2007), the mixing effects due to the presence of non-axisymmetric structures (e.g. central bar, long-lived spiral arm; e.g. Andrievsky et al. 2004; Scarano & Lépine 2013), or by a merger event (e.g. Yong et al. 2005).

Out of the midplane, the radial gradients are found to flatten or even reverse to a positive slope as the height from the midplane increases (Allende Prieto et al. 2006; Jurić et al. 2008; Carrell et al. 2012; Cheng et al. 2012; Hayden et al. 2014). The flattening of the radial gradient is possibly linked to the distributions of different stellar populations in the Galactic disk(s) and may possibly be explained by the different levels of mixture of thin- and thick-disk stars as height varies (e.g. Jurić et al. 2008). The vertical gradients have also been found to show spatial variations in the sense that the gradients flatten with increasing R_{GC} (e.g. Hayden et al. 2014).

The evolution of radial gradient is of utter importance for an understanding of the formation and evolution of the Galactic disk(s). However, the results of existing studies on temporal variations of the radial gradient of the disk are far from being unequivocal, both observationally and theoretically. Most studies based on OCs have found a flattening radial gradient with cosmic time by dividing the OCs into different age bins. The results from PNe are less clear: the flattening, steepening and unchangingness are all reported in the literature (e.g. Maciel et al. 2005; Stanghellini & Haywood 2010; Henry et al. 2010). It should be emphasized that all the tracers (OCs/PNe) used in the above analyses are younger than about $5-7$ Gyr (see Maciel et al. 2005). The situation of possible radial gradient evolution at the early epochs of disk formation is still unclear. Theoretically, different chemical evolution models predict different evolutions of the radial gradient: flattening with cosmic time (e.g. Mollá et al. 1997; Portinari & Chiosi 1999; Hou et al. 2000) or steepening with cosmic time (e.g. Tosi 1988; Chiappini et al. 1997, 2001). More recently, radial migration has been suggested to be an important process in regulating the evolution of the radial gradient and thus has to be included in chemical evolution models (e.g. Schönrich & Binney 2009; Loebman et al. 2011; Kubryk et al. 2013; Minchev et al. 2013). Generally, the radial gradients of old populations will be strongly affected and flattened by the migration.

Compared to measurements of the exact slope of the metallicity gradient, studies of the spatial and temporal variations of the gradients are more fundamental for understanding the formation and evolution of the Galactic disk(s) since the variations contain information about the underlying physical processes that regulate the disk formation and evolution at different times, and in different regions of the disk. However, as described above, the currently available measurements of the spatial and temporal variations of the gradients are still quite controversial and in doubt. This is possibly because most of the previous studies have not considered the temporal variations of gradients when deriving the spatial variations of gradients, or the spatial variations of gradients when deducing the temporal variations of gradients, given the following considerations. Firstly, the metallicity gradients in different regions of the disk may vary significantly, due to, for example, the effects of non-axisymmetric perturbations or merger events. Secondly, as discussed earlier, different tracers probe metallicity gradients at different evolutionary epochs of the Galaxy. Finally, the potential biases caused by target selection effects are not always fully explored in many of the existing studies. This last effect is, at least partly, responsible for the differing results yielded by different studies. A large-scale spectroscopic survey that targets large numbers of stars over the full age range of the Galaxy and covers a sufficiently large volume of the Galactic disk(s) with sufficient sampling number density, for all stellar populations concerned, is thus required to address the above problems properly and eventually draw a clear picture about how the Galactic disk(s) forms and evolves chemo-dynamically.

The Large Sky Area Multi-Object Fiber Spectroscopic Telescope[1] (LAMOST, also named the Guo Shou Jing Telescope) Spectroscopic Survey of the Galactic Anti-center (LSS-GAC; Liu et al.

---

[1] LAMOST is a 4 meter quasi-meridian reflecting Schmidt telescope equipped with 4000 fibers, each having an angular diameter of 3.3 arcsec projected on the sky, distributed in a circular field of view of 5° in diameter (Cui et al. 2012).

2014), as a major component of the ongoing LAMOST Experiment for Galactic Understanding and Exploration (LEGUE; Deng et al. 2012; Liu et al. 2015). This project aims to collect low resolution ($R \sim 1800$), optical ($\lambda\lambda\, 3800 - 9000$) spectra under dark and grey lunar conditions for a statistically complete sample of over 3 million stars with magnitudes $14.0 \leq r \leq 17.8$ mag (down to 18.5 mag for limited fields), in a contiguous sky area of ~ 3400 square degrees, centered on the Galactic Anticenter (GAC), covering Galactic longitudes $150 < l < 210°$ and latitudes $|b| < 30°$. Over 1.5 million spectra of very bright stars ($9 < r < 14.0$ mag) will also be obtained under bright lunar conditions. The survey will deliver spectral classifications, values of stellar radial velocity V_r and stellar atmospheric parameters (effective temperature T_{eff}, surface gravity $\log g$, metallicity [Fe/H], [α/Fe] and [C/Fe]) from the collected spectra. As designed, the survey will provide a large number of stars, of the order of a few million, with a contiguous sky coverage of a large area of the Galactic disk(s) with a relatively high sampling density (hundreds of stars per square degree) yet using a simple but nonetheless nontrivial target selection algorithm (random selection in the color–magnitude diagram, i.e. r versus $g - r$ and r versus $r - i$). The survey will thus enable simultaneous measurements of the radial and vertical metallicity gradients across a large volume of the Galactic disk(s). The LSS-GAC regular survey was initiated in September 2012. It is expected to last for five years.

Based on the large stellar spectroscopic samples obtained by the LSS-GAC, we have started a series of investigations to systematically study the spatial and temporal variations of metallicity gradients in the Galactic disk(s). Xiang et al. (2015c, hereafter Paper I) examine the spatial and temporal variations (in both radial and vertical directions) of metallicity gradients for $7.5 < R_{\mathrm{GC}} < 13.5$ kpc and $|Z| < 2.5$ kpc using a sample of nearly 0.3 million main-sequence turnoff (MSTO) stars with ages ranging from 2 to over 11 Gyr, selected from the LSS-GAC Data Release 2 (DR2) (Xiang et al. 2015d, in preparation) The current study, the second one of this series, also selects over 70 000 red clump (RC) giants with intermediate- to old-ages from the LSS-GAC DR2. The bright intrinsic luminosities of RC stars allow us to investigate the (radial and vertical) gradients over a slightly larger volume of the disk, covering $7.0 < R_{\mathrm{GC}} < 14.0$ kpc and $|Z| < 3.0$ kpc, than possible with the MSTO star sample used by Paper I. The current sample is thus particularly suitable for the study of the outer disk and provides a unique opportunity to address the question of whether the radial gradient of the outer disk is flatter than that near the solar circle as described above.

The paper is organized as follows. We describe in detail the selection of the RC sample in Section 2. We present our results in Section 3, followed by discussions in Section 4. Conclusions are given in Section 5.

2 DATA AND SAMPLE SELECTION

2.1 Data

The data used in the current study are mainly collected during the pilot (Sep. 2011 – Jun. 2012) and first-two-year (Sept. 2012 – Jun. 2014) regular surveys of LSS-GAC. The stellar radial velocity V_r and stellar atmospheric parameters (T_{eff}, $\log g$, [Fe/H]) are determined with the LAMOST Stellar Parameter Pipeline at Peking University (LSP3; Xiang et al. 2015a,b), and have an overall accuracy of 5–10 km s^{-1}, 150 K, 0.25 dex and 0.15 dex, respectively, for a spectral signal-to-noise ratio (S/N) per pixel (~ 1.07 Å) at 4650 Å (S/N (4650 Å)) ≥ 10. Stellar parameters, together with values of interstellar extinction and stellar distance estimated with a variety of techniques for over 0.7 million stars observed in the pilot and first-year regular surveys are now publicly available as the first data release of the value-added catalog of LSS-GAC (LSS-GAC DR1; Yuan et al. 2015). The data of another 0.7 million stars with S/N (4650 Å) ≥ 10 from the second-year regular survey will soon be publicly available as the second release of the value-added catalog of LSS-GAC (Xiang et al. 2015d, in preparation). In addition to the LSS-GAC data, the current study has also included about 80 000 stars from the spheroid parts ($|b| > 20°$) of LEGUE and 50 000 stars from the LAMOST–*Kepler* Field Survey (De Cat et al. 2014). The latter are particularly useful for the RC selections (see

Sect. 2.2). The additional spectra from the latter two surveys are also processed in the same way as for the LSS-GAC sources with the LSP3.

2.2 The RC Sample

2.2.1 An overview of RC stars

The helium burning RC stars[2] are an easily recognizable feature in the color-magnitude diagram (CMD) of intermediate- to old-age stellar populations that are low-mass but metal-rich. RC stars are considered to be standard candles since their absolute luminosities are fairly independent of their stellar chemical composition and age (e.g. Cannon 1970; Paczyński & Stanek 1998). With an accurate calibration of absolute magnitudes from several hundred local RC stars using the *Hipparcos* (ESA (1997)) parallaxes that have become available, RC stars have become popular distance indicators and have been widely used to obtain precise distances to the Galactic Center (Paczyński & Stanek 1998) and the Local Group of galaxies (e.g. LMC by Laney et al. 2012; M31 by Stanek & Garnavich 1998). The key to this method is a notable over-density feature easily identifiable in the CMD of stars in those distant objects due to the presence of a large number of RC stars at nearly the same distance.

However, identifying individual RC stars among the numerous field stars is not an easy task. Field RC stars are spread over a wide range of distances and there is no apparent over-density in the CMD of field stars that can be used to single out the RC members. Fortunately, high-resolution spectroscopic analysis of nearby RC stars shows that they are distributed in a relatively "small box" in the T_{eff}–$\log g$ diagram (i.e. HR diagram) of $4800 \leq T_{\text{eff}} \leq 5200$ K and $2.0 \leq \log g \leq 3.0$ (e.g. Puzeras et al. 2010). This is simply because T_{eff} is an excellent proxy of stellar color whereas $\log g$ is sensitive to the stellar absolute luminosity. Recently, with values of T_{eff} and $\log g$ available from large-scale spectroscopic surveys that include large numbers of field stars, it has become feasible to select a large number of field RC candidates. RC candidates thus selected have been widely used to study the metallicity gradients and stellar kinematics of the Galactic disk(s) (e.g. Siebert et al. 2011; Bilir et al. 2012; Williams et al. 2013; Bienaymé et al. 2014). However, stars falling inside that "small box" are not purely RC stars and have significant ($\sim 60\%$; Williams et al. 2013) contamination from the red giant branch (RGB). The differences in absolute magnitudes between RC and RGB stars can be larger than 1 mag and this can lead to large systematic errors in distances for the selected RC sample stars. More recently, a new method has been proposed by Bovy et al. (2014, hereafter B14) to select a clean RC sample from large-scale spectroscopic data. The method first separates the RC-like and RGB stars using cuts on a metallicity-dependent T_{eff}–$\log g$ diagram, assisted by using stellar isochrones and calibrated with high quality *Kepler* asteroseismic $\log g$ (e.g. Creevey et al. 2013) as well as high precision stellar atmospheric parameters from the APOGEE survey (Pinsonneault et al. 2014). Second, secondary RC stars (i.e. high mass helium burning stars ignited non-degenerately) are then removed from the RC-like stars via cuts on a metallicity (Z)–color $(J - K_{\text{s}})_0$ diagram. The expected purity of the final RC sample is $\geq 93\%$ and the typical distance errors are within 5– 10%. The key point of this new method in selecting a clean RC sample is accurate values of surface gravity $\log g$. Unfortunately, it is difficult to apply this method to the current LSS-GAC data given the relatively large systematic plus random errors ($\sim 0.2 - 0.4$ dex) of $\log g$ estimates delivered by the LSP3, as shown by a recent comparison of LSP3 and asteroseismic $\log g$ values for common objects in the LAMOST–*Kepler* fields (Ren et al. 2015, in preparation). As we shall show later (Section 2.2.2) there are also significant deviations between T_{eff}–$\log g$ values yielded by the LSP3 and those predicted by the PARSEC stellar isochrones (Bressan et al. 2012) of LSS-GAC DR2 red

---

[2] RC stars of interest here refer to those in which the helium burning is ignited following a helium flash that breaks the degeneracy of the helium core.

giant stars for a typical metallicity [Fe/H] = -0.3. Therefore, for selecting a clean RC sample from the LSS-GAC data set, it is necessary to improve the accuracy of LSP3 $\log g$ estimates.

2.2.2 Re-determinations of LSP3 $\log g$ estimates with the KPCA algorithm

Asteroseismology is very powerful for determining stellar surface gravity $\log g$, and is capable of yielding values much more accurate than possible with the traditional spectroscopic method. Thanks to the *Kepler* mission (Borucki et al. 2010), asteroseismic values of $\log g$ for tens of thousands stars are now available, with a typical error of ~ 0.02 dex (Huber et al. 2014). This number of stars is however still orders of magnitude smaller than those that have already been targeted by large-scale spectroscopic surveys, including LSS-GAC. It will be thus very useful to calibrate and improve the accuracy of spectroscopic estimates of $\log g$ using the much more accurate asteroseismic values. Very recently, Liu et al. (2015) improved the accuracy (by a factor of two) of $\log g$ estimates produced by the LAMOST Stellar Parameter Pipeline (LASP; Wu et al. 2011; Luo et al. 2015) using a support vector regression model trained by asteroseismic $\log g$ measurements of thousands of giants from the LAMOST–*Kepler* fields. Here, a similar effort is presented for the LSP3 $\log g$ estimates. We re-determine and improve the accuracy of LSP3 estimates of $\log g$ based on a Kernel Principal Component Analysis (KPCA; Schölkopf et al. 1998) method trained with thousands of giants in the LAMOST–*Kepler* fields with accurate asteroseismic $\log g$ measurements.

Principal Component Analysis (PCA) is a classical statistical method that can convert observations (e.g. spectra) into a set of linearly uncorrelated orthogonal variables or principal components (PCs). The method has widely been used to estimate stellar atmospheric parameters (e.g. Singh et al. 1998; Rees et al. 2000; Re Fiorentin et al. 2007). KPCA keeps the concept of PCA but it can be extended to nonlinear feature extraction using kernel techniques. Considering the nonlinear dependence of spectral features on $\log g$, KPCA is more suitable than the standard PCA method for the case of $\log g$ estimation.

To apply the KPCA method to the $\log g$ determinations for a whole spectroscopic sample, it is necessary to construct a tight relation between the LAMOST spectra (at the present, only the blue-arm spectra[3] between $3930 \leq \lambda \leq 5500$ Å are used) and the corresponding asteroseismic values of $\log g$ with training data. To build up a training sample, we have cross matched our sub-sample of about 50 000 stars in the LAMOST–*Kepler* fields with the currently available largest asteroseismic $\log g$ (hereafter $\log g_{AST}$) sample ($\sim 16\,000$ stars) from Huber et al. (2014). In total 3562 common sources with spectral S/N (4650 Å) ≥ 10 are identified. For self-consistency, we have used the LSP3 estimates of T_{eff} and the observed frequencies with maximum power (ν_{max}) from Huber et al. (2014) to re-estimate values of $\log g$ for the 3562 common sources, using the asteroseismic scaling relation $\nu_{max} \propto g\,T_{eff}^{-0.5}$ (Brown et al. 1991; Belkacem et al. 2011). We then trim this sample of common sources by requiring that LSP3 $\log g \leq 3.8$, $3500 \leq T_{eff} \leq 6000$ K and [Fe/H] ≥ -1.0, for the following three reasons: (1) The current study is mainly interested in the estimation of $\log g$ for red giant stars including RGB and RC stars; (2) Currently only a small number of dwarfs have asteroseismic determinations of $\log g$; and finally, (3) The surface gravity of metal-poor stars with [Fe/H] < -1.0 is currently poorly determined by the astroseismic scaling relation (Epstein et al. 2014). The trimming leaves 3267 sources. The 3267 sources are then further divided into two groups: a training sample and a control sample. For the training sample, we select 1355 stars with spectral S/N (4650 Å) ≥ 50 to minimize the effects of spectral noises and of errors in LSP3 stellar atmospheric parameters T_{eff}

---

[3] In principle, red-arm spectra should also be included given that the stars of concern here are mainly red giants that are bright in the red and thus generally have high spectral SNRs. However, considering that the sky subtraction of the current LAMOST 2D pipeline (Luo et al. 2015) still suffers from some problems in the red and the fact that most stars typically have few spectral features in red, we have opted to consider the blue-arm spectra in the current study. In the future, with improved sky subtraction, we expect that including the red-arm spectra can help improve the results.

and [Fe/H] in the training process. The remaining 1912 stars constitute the control sample, which will be used to test the accuracy of $\log g$ determined with the KPCA algorithm.

To extract information on stellar surface gravity from the LAMOST spectra, we assume a KPCA model (with a Gaussian kernel) that has 25 PCs, $N_{\mathrm{PC}} = 25$, when constructing the relation between $\log g_{\mathrm{AST}}$ and the LAMOST blue-arm spectra with the training sample. $N_{\mathrm{PC}} = 25$ is chosen in the KPCA model to achieve a tradeoff between reducing the training residual and retaining a relatively high accuracy in the estimate of $\log g$ for LAMOST spectra at low values of spectral S/N (see Appendix A). In the training process, T_{eff} and [Fe/H] are fixed to the value yielded by the LSP3. The model fits the data well, generating residuals of only $\sim$0.1 dex, as shown in Figure 1. In addition, the figure shows that the residuals exhibit no obvious systematic trend as the LSP3 T_{eff} and [Fe/H] vary. However, we caution that the residuals show a weak trend as the asteroseismic $\log g$ varies from 2.5 to 3.5. The reason is unclear but the trend does not affect the selection of RC stars (see Fig. 5). To test the accuracy of KPCA $\log g$ values, we use the relation generated by the training sample applied to the control sample. The results are shown in Figure 2. The differences between KPCA and asteroseismic $\log g$ are less than 0.15 dex for spectral S/N $(4650\,\text{Å}) > 18$ and less than 0.10 dex for S/N $(4650\,\text{Å}) > 30$. Thus the accuracy of KPCA $\log g$ estimates are about a factor of two better than the LSP3 values. The test shows that there are no obvious systematics over the whole parameter space (atmospheric parameters as well as S/N ratios) spanned by the control sample.

We now apply the above model to the LAMOST blue-arm spectra and re-determine $\log g$ values for all LSS-GAC DR2 red giants[4] using the relation constructed from the training sample. This yields newly derived KPCA $\log g$ values for over 0.35 million LSS-GAC DR2 red giants[5] with spectral S/N $(4650\,\text{Å}) > 10$. As another test of the accuracy of the newly derived KPCA $\log g$ estimates, we plot the differences of KPCA $\log g$ values yielded by ~ 6500 pairs of duplicate observations with similar S/N $(4650\,\text{Å})$ as a function of S/N in Figure 3. The results are quite similar to those found for the control sample. Again, this indicates that our newly derived KPCA $\log g$ values are about a factor of two more accurate than those of LSP3. We also find that the HR diagram constructed using the LSP3 T_{eff} and the newly derived KPCA $\log g$ for our sample stars is in excellent agreement with the prediction of the PARSEC stellar evolution model, as shown in Figure 4. As mentioned before, the position of the RC clump in the original HR diagram constructed with LSP3 T_{eff} *and* $\log g$ deviates significantly from that predicted by the PARSEC model.

2.2.3 Selection of RC stars

As described above, the newly derived KPCA $\log g$ values, with much improved accuracy (both in random and systematic errors), have greatly reduced the differences between the observed and predicted position and morphology of the RC clump on the HR diagram, thus enabling us to select a clean RC sample following the method proposed by B14. First, to obtain a set of cuts that distinguish RC from RGB stars on the $T_{\mathrm{eff}} - \log g$ diagram, we cross-identify red giants from the LAMOST-*Kepler* fields with those from Stello et al. (2013), in which the evolutionary stages of stars have been classified based on the frequencies and spacings of the gravity-mode measured from the *Kepler* light curves. This leads to 600 stars in common with LAMOST spectral S/N $(4650\,\text{Å}) \geq 40$ (hereafter the LAMOST-EVOLUTION sample or LE sample for short). The S/N cut is to ensure that the stellar atmospheric parameters are accurate enough, especially the KPCA $\log g$ values (better than 0.1 dex under this cut). The LE sample stars are mostly classified by Stello et al. (2013) as either 'RC' or 'RGB,' with only a few classified as 'UNKNOWN'. Unlike B14, who use cuts defined with the asteroseismic and spectroscopic estimates of $\log g$ values, we opt to define the cuts using the LE

---

[4] Red giants are selected from the whole LSS-GAC DR2 sample using the same set of stellar atmospheric parameter cuts as for the training sample, i.e. $\log g \leq 3.8$, $3500 \leq T_{\mathrm{eff}} \leq 6000\,\text{K}$ and [Fe/H] ≥ -1.0.

[5] This includes targets from the LSS-GAC as well as stars from the spheroid part of the LEGUE and the LAMOST–*Kepler* fields.
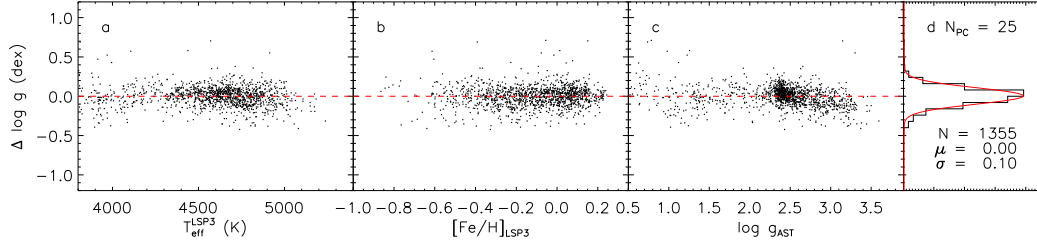
Fig. 1 Distributions of values of residuals, $\log g_{\rm KPCA} - \log g_{\rm AST}$, of the training sample as a function of LSP3 $T_{\rm eff}$ and [Fe/H] (*panels a and b*, respectively) and of asteroseismic $\log g$ (*panel c*). Panel (d) shows a histogram distribution of the residuals (*black line*). Also overplotted in red is a Gaussian fit to the distribution. The mean $\mu = 0.00$ dex and dispersion $\sigma = 0.10$ dex of the fit, as well as the number of stars used, $N = 1355$, are marked. For the current KPCA analysis, $N_{\rm PC} = 25$ is assumed. See the text for details.
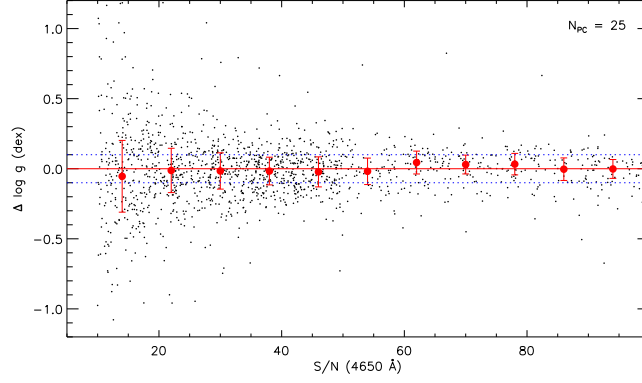
Fig. 2 Differences in the KPCA $\log g$ estimates and asteroseismic values for the control sample, plotted as a function of spectral S/N (4650 Å). The blue dashed lines indicate differences $\Delta \log g = \pm 0.1$ dex. The means and standard deviations of the differences in the individual S/N (4650 Å) bins (binsize = 8) are oveplotted with dots and error bars, respectively. Again, $N_{\rm PC} = 25$ is assumed.
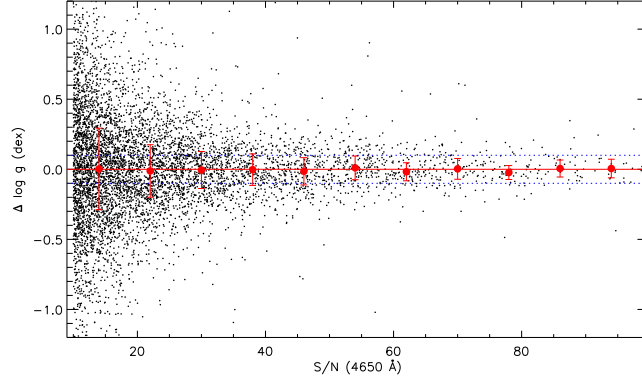

Fig. 3 Differences of KPCA $\log g$ estimates produced by duplicate observations with similar S/N (4650 Å) plotted as a function of S/N (4650 Å). The blue dashed lines indicate differences $\Delta \log g = \pm 0.1$ dex. The means and standard deviations of the differences in the individual S/N (4650 Å) bin (binsize = 8) are oveplotted as red dots and error bars, respectively. Again, $N_{\rm PC} = 25$.

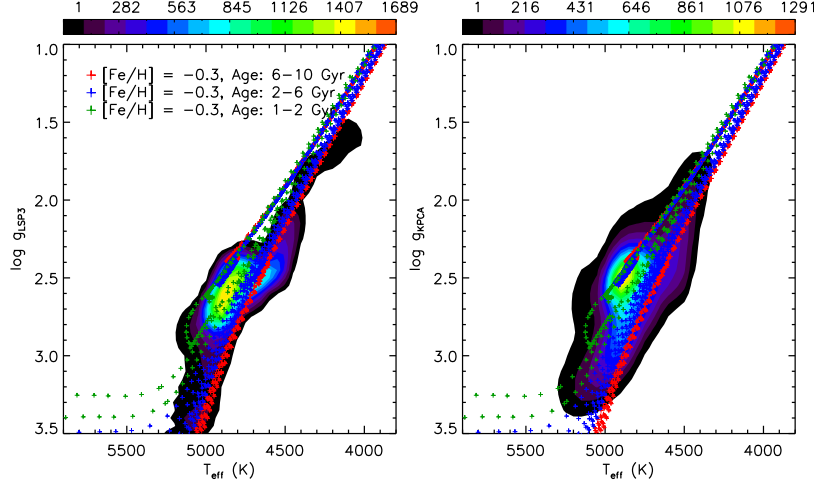**Fig. 4** Pseudo-color HR diagrams of red giant stars from the LSS-GAC DR2. Only stars with LSP3 metallicity [Fe/H] between -0.4 and -0.2 (where the metallicity distribution of our red giant sample peaks) are included. Effective temperatures are those given by the LSP3. In the left panel, $\log g$ values are from the LSP3, whereas those in the right panel are newly derived with the KPCA method. Also overplotted are the PARSEC stellar isochrones for [Fe/H] $= -0.3$. Different colors represent different stellar ages (1–2 Gyr, *green crosses*; 2–6 Gyr, *blue crosses*; 6–10 Gyr, *red crosses*).

sample, relying directly on $\log g$ values determined with the KPCA method, together with T_{eff} and [Fe/H] yielded by the LSP3. With this change, there is neither the need to introduce an additional cut that corrects for the systematic difference between the asteroseismic and spectroscopic estimates of $\log g$ (e.g. the additional cut given by eq. (9) in B14), nor the need to account for the possible systematic differences between the PARSEC and spectroscopic values of the other atmospheric parameters (T_{eff} and [Fe/H]). The cuts defined here are therefore more straightforward and appropriate for real observed data.

Figure 5 compares the distribution on the $T_{\text{eff}} - \log g$ HR diagram of the LE sample stars with that predicted by the PARSEC stellar isochrones for two metallicity bins. The predicated distribution is generated assuming, similar to B14, a lognormal Chabrier (2001) for an initial mass function (IMF), a constant star formation history (SFH) with ages less than 10 Gyr and a metallicity distribution function (MDF) that matches that of the LE sample stars in the two metallicity bins. As Figure 5 shows, the distribution of RC-like stars, with $\log g$ values roughly between 2.5 and 2.9, and that of RGB stars, as classified by Stello et al. (2013), is roughly in agreement with the predicted distribution from the PARSEC stellar evolution model except for some small systematic differences between the LSP3 and PARSEC values of T_{eff}, and is well separated from that of RGBs as well. Finally, ignoring those stars classified as an 'UNKNOWN' evolutionary stage, we derive the following cuts as given by the following two equations that maximize the product of completeness f_{comp} ($\equiv N_{\text{RC}}^{\text{Sel}}/N_{\text{RC}}^{\text{All}} \sim 96\,\%$) and purity f_{purity} ($\equiv 1 - N_{\text{RGB}}^{\text{Sel}}/N_{\text{All}}^{\text{Sel}} \sim 95\,\%$),

$$1.8 \leq \log g \leq 0.0009\,\text{dex}\,\text{K}^{-1}\left\{T_{\text{eff}} - T_{\text{eff}}^{\text{Ref}}([\text{Fe/H}])\right\} + 2.5\,, \tag{1}$$

where

$$T_{\text{eff}}^{\text{Ref}}([\text{Fe/H}]) = -876.8\,\text{K}\,\text{dex}^{-1}\,[\text{Fe/H}] + 4431\,\text{K}\,. \tag{2}$$

Table 1 Values of purity and completeness in selection of RC-like stars under different uncertainties in errors of $\log g$ measurements for the cuts given by Eqs. (1) and (2).

$\sigma_{\log g}$ (dex)	0.1	0.15	0.20	0.25	0.30
S/N[a]	> 40	20	18	15	10
f_{purity}	$94 \pm 1\%$	$89 \pm 1\%$	$83 \pm 2\%$	$78 \pm 2\%$	$74 \pm 2\%$
f_{comp}	$96 \pm 1\%$	$90 \pm 2\%$	$83 \pm 2\%$	$78 \pm 2\%$	$74 \pm 3\%$

Notes: [a] S/N ratios required by the KPCA method to achieve the corresponding uncertainties in $\log g$ measurements listed in the first row of the table.

$N_{\text{RC}}^{\text{All}}$ represents the total number of real RC stars, and $N_{\text{RC}}^{\text{Sel}}$ and $N_{\text{RGB}}^{\text{Sel}}$ the numbers of RC and RGB stars that pass the cuts of Equations (1) and (2), respectively. $N_{\text{All}}^{\text{Sel}}$ is the sum of $N_{\text{RC}}^{\text{Sel}}$ and $N_{\text{RGB}}^{\text{Sel}}$, which represents the total number of stars passing the cuts.

Figure 5 shows that the cuts developed by B14 (green lines in the figure) are not fully suitable for our data because their cuts reject some real RC stars in the lower temperature range but include some RGB stars as RC stars in the higher temperature range. We have also plotted Figure 5 using the asteroseismic values of $\log g$ from Huber et al. (2014) for the LE sample stars but did not find any significant difference from what is shown here. This indicates the difference between our current cuts and those of B14 cannot be caused by the usage of KPCA $\log g$. This difference in cuts is possibly caused by the systematic differences in values of T_{eff} as yielded by the LSP3 and given by PARSEC, as mentioned earlier.

To examine the performance of our cuts for different errors in $\log g$ measurements, we use a Monte Carlo method to simulate the selection process under different errors in $\log g$ and derive the corresponding values of f_{comp} and f_{purity}. Here we assume that the uncertainties in the LE sample stars have a minimum value of 0.1 dex (almost the best accuracy achievable using the KPCA method), based on the test results presented in Section 2.2.2 using the control sample and duplicate observations. Values of f_{comp} and f_{purity} for larger errors are then derived by randomly assigning larger errors to $\log g$ values of the LE stars and repeating the selection with Equations (1) and (2) 10 000 times. The results are presented in Table 1. In Table 1, we have also listed the spectral S/N (4650 Å) ratios required by the KPCA method in order to achieve the listed uncertainties of $\log g$ measurements. With the cuts developed in the current work, the amount of contamination from RGB stars is half that of the selection using a "small box" such as what was adopted by Williams et al. (2013). Even with $\log g$ having measurement uncertainties as large as 0.3 dex, a good accuracy is achievable with the KPCA method for a spectral S/N (4650 Å) ratio as low as 10.

As shown in Figure 5, the region where RC-like stars fall shows two distinct features: a clump of stars with almost constant $\log g = 2.5$ and $4600 \leq T_{\text{eff}} \leq 4850$ K (i.e. the main RC stars) and a skewed tail of stars with $2.5 \leq \log g \leq 2.9$ and $4800 \leq T_{\text{eff}} \leq 5000$ K (i.e. the secondary RC stars with fainter luminosities). The secondary RC stars are not standard candles and their luminosities are a function of mass (age). We need to remove them from our RC-like star sample to ensure that the distances provided by the sample stars can be determined precisely and simply.

To remove secondary RC stars and low surface gravity RGB stars, we adopt the color $(J - K_{\text{s}})_0$–metallicity Z^6 cuts as developed by B14 using the PARSEC stellar evolution model. The cuts try to select stars that have a nearly constant absolute magnitude with 1σ dispersion ≤ 0.1 mag and eliminate those non-standard candles, including secondary RC, RGB and AGB stars. For a more detailed description, please refer to section 2.2 of B14. Since the cuts are purely based on the stellar evolution model, empirical examination is required to eliminate potential discrepancies, if any, between the model and observations. To test the cuts, we again use the LE sample. For consistency, we first apply the cuts of B14 on the $T_{\text{eff}} - \log g$ diagram to the LE sample to select

---

[6] Z is converted from [Fe/H] using the equation given by Bertelli et al. (1994), assuming $Z_\odot = 0.017$.
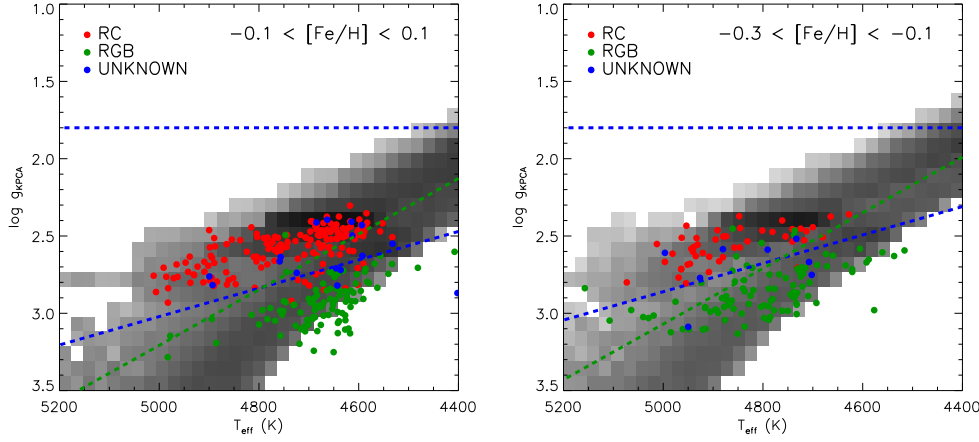
Fig. 5 Distribution of stars on the $T_{\mathrm{eff}} - \log g$ HR diagram predicted by the PARSEC stellar evolution model with assumptions as described in the text (grey scale), compared to those of the LE sample stars (*colored points*), for two metallicity bins as marked. Values of T_{eff} and [Fe/H] for the LE sample stars are from LSP3 and those of $\log g$ from the KPCA method. Red, magenta and blue points represent stars in the RC, RGB and unknown evolutionary stages, as classified by Stello et al. (2013), respectively. The blue dashed lines represent the cuts that separate RC stars from the less luminous RGB stars as given in Eqs. (1) and (2). The green dashed lines give the cuts adopted by B14.
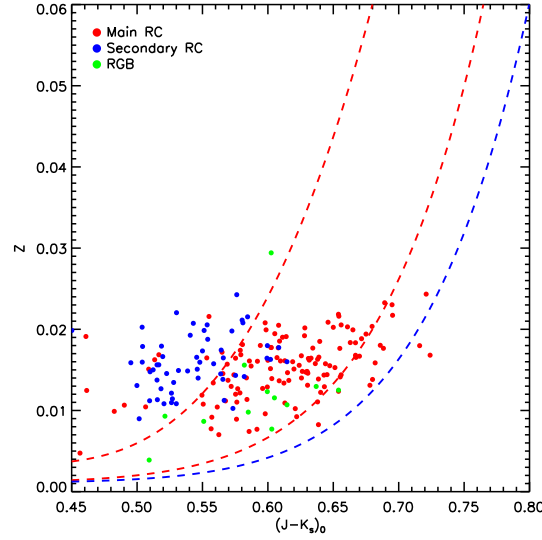
Fig. 6 Distribution of RC-like stars in the color $(J - K_{\mathrm{s}})_0 - Z$ plane, using 2MASS photometric measurements and LSP3 metallicities. Dots in red, blue and green represent the main RC, secondary RC and RGB stars, respectively. The red dashed lines are developed by B14 to eliminate the contamination of secondary RC stars. The blue dashed line is our revised cut developed in the current study as a replacement for the lower red dashed line.

RC-like stars using the asteroseismic $\log g$ values. After correcting for the interstellar extinction as estimated with the 'star pair' method (see Yuan et al. 2015), the distribution of selected RC-like stars in the $(J - K_{\mathrm{s}})_0 - Z$ plane is shown in Figure 6. The photometric magnitudes of the stars are taken from 2MASS (Skrutskie et al. 2006) and their metallicities from the LSP3. By definition, secondary RC stars have masses $\geq 2\,M_\odot$ and main RC stars have masses $< 2\,M_\odot$. Again with masses also estimated by Stello et al. (2013), we divide the RC-like stars into two groups: main and secondary RC stars. As Figure 6 shows, the contamination of RGB stars, as expected, is negligible but that of secondary RC stars is significant. Luckily, compared to main RC stars, secondary RC stars belong to a young and metal-rich population with large masses. As a consequence, they occupy the bluer and more metal-rich part of the color–metallicity diagram. Main and secondary RC stars can be well separated using a cut given by the following equation as proposed by B14 (the upper red dashed line in Fig. 6),

$$Z < 2.58[(J - K_{\mathrm{s}})_0 - 0.400]^3 + 0.0034 \,. \tag{3}$$

However, Figure 6 also shows that the lower cut of B14 (the lower red dashed line in Fig. 6), designed to reject RGB stars with high surface gravity, seems to also eliminate a considerable fraction of real main RC stars. This is possibly caused by discrepancies between model and observations. To correct for this, we adjust the lower cut of B14 to (the blue dashed line in Fig. 6),

$$Z > 1.21[(J - K_{\mathrm{s}})_0 - 0.085]^9 + 0.0011 \,. \tag{4}$$

2.2.4 The RC sample

With T_{eff} and [Fe/H] estimated with the LSP3, $\log g$ derived with the KPCA method and $(J - K_{\mathrm{s}})_0$ calculated from 2MASS photometry[7] after being corrected for extinction as estimated with the 'star pair' method (Yuan et al. 2015), we apply the cuts defined by Equations (1)–(4) to the LSS-GAC DR2 red giant sample and obtain a clean RC sample of about 0.11 million stars with S/N $(4650\,\text{Å}) \geq 10$. The distances of these RC stars are derived using the recent calibration, $M_{K_{\mathrm{s}}} = -1.61$ mag, for a nearby RC sample (Laney et al. 2012)[8]. Since the intrinsic scatter in absolute magnitudes of RC stars is estimated to be within 0.1 mag, the distances derived are expected to have uncertainties no more than $5 - 10\,\%$, given a typical photometric error of ~ 0.05 mag in the K_{s}-band and an extinction error of ~ 0.04 mag in $E(B - V)$ (see Yuan et al. 2015). Proper motions of the sample stars are taken from the UCAC4 (Zacharias et al. 2013) and PPMXL (Roeser et al. 2010) catalogs. Given the high precision in distance and large spatial coverage (Fig. 7) of the current RC star sample, it is not only useful to address the problem of metallicity gradients in the Galactic disk of concern here, but can also be used to tackle a variety of problems with regard to Galactic structures and dynamics. The sample will be made publicly available at the website: (*http://162.105.156.249/site/data/RC_Sample*).

In order to obtain accurate metallicity gradients of the Galactic disk(s) of concern here, we restrict the current analysis to a subset of the RC sample stars with S/N $(4650\,\text{Å}) > 15$, to ensure a sufficiently high accuracy of [Fe/H] determinations, and to eliminate possible contaminations from halo stars with [Fe/H] ≤ -1.0 dex (which is also the lowest range of [Fe/H] that the KPCA method can be applied for $\log g$ estimates). Finally, a total of 74 280 unique RC stars are selected. The number density distributions of this adopted sample of RC stars in the $X - Y$ and $X - Z$ Galactic planes are presented in Figure 7. Here X, Y and Z are coordinates of a right-handed Cartesian coordinate system with its origin at the Galactic center. The X-axis passes through the Sun and points towards the Galactic Center, the Y-axis is in the direction of Galactic rotation and the Z-axis points towards the North Galactic Pole. The Sun is located at $(X, Y, Z) = (-R_0, 0, 0)$, where $R_0 = 8$ kpc.

---

[7] Only stars with *ph_qual* flagged as 'A' in both J and K_{s} bands are included.

[8] B14 assign absolute magnitudes to RC stars based on their positions in the $(J - K_{\mathrm{s}})_0 - Z$ plane. However, we find that the absolute magnitudes of RC stars predicted by the stellar evolution model are almost constant except for those super metal-rich cases ($Z \geq 0.04$, i.e. [Fe/H] $\geq 0.4 - 0.5$ dex; see fig. 3 of B14), which are very rare in our RC sample.
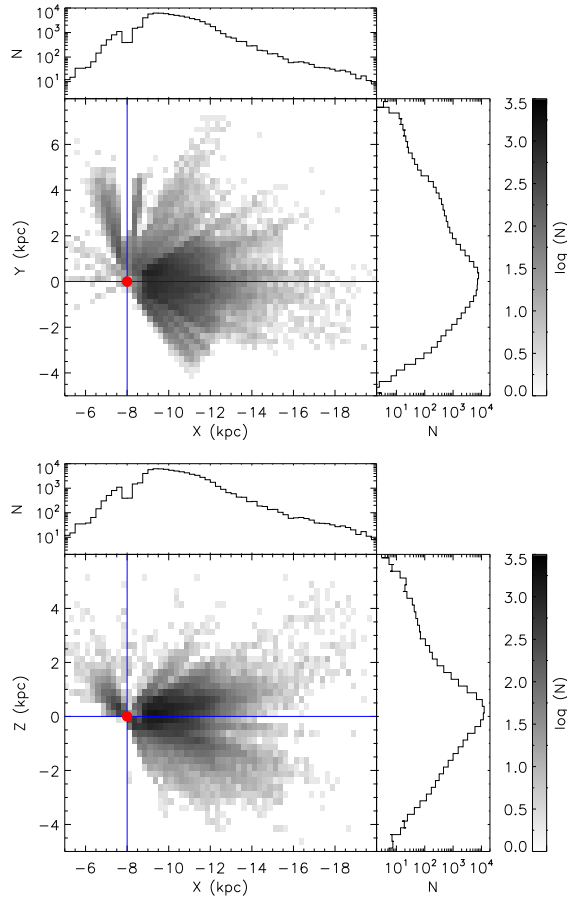
Fig. 7 Greyscale number density distribution of RC sample stars in the $X - Y$ (*left panel*) and $X - Z$ (*right panel*) planes. The Sun is located at $(X, Y, Z) = (-8.0, 0.0, 0.0)$ kpc. The stars are binned by 0.25×0.25 kpc^2 in both diagrams. The densities are shown on a logarithmic scale. Histogram distributions along the X, Y and Z axes are also plotted.
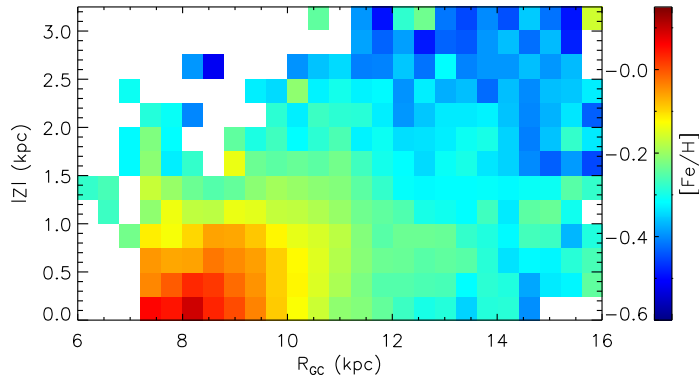

Fig. 8 Mean metallicity [Fe/H] as a function of R_{GC} and $|Z|$ deduced from our RC sample, binned by 0.40×0.25 kpc^2 in R_{GC} and $|Z|$, respectively.

As Figure 7 shows, our RC sample covers a volume of $-16 \leq X \leq -6$ kpc, $-4 \leq Y \leq 5$ kpc and $-3 \leq Z \leq 3$ kpc.

We note that the current RC sample is largely a magnitude limited sample. Considering that the absolute magnitudes of RC stars are quite insensitive to both metallicity and age, we believe that any potential population effects that may be present in our sample are unlikely to significantly affect the metallicity gradients derived from this sample. In addition, the cuts that define the RC sample in the current selection exclude stars with ages younger than 1 Gyr (i.e. those relatively massive and young secondary RC stars) and halo stars with metallicities poorer than -1.0 dex. The current sample is expected to be mainly composed of intermediate-age stars with typical ages between 1.0 and 4.0 Gyr if one assumes a flat SFH and a solar-neighborhood MDF (Casagrande et al. 2011; see section 5 of B14 for a more detailed discussion).

3 RESULTS

3.1 Spatial Distribution of Mean Metallicities

The spatial distribution of mean metallicities of the RC sample in 0.40×0.25 kpc^2 bins, with at least five stars in each bin, in terms of the projected Galactocentric radius (R_{GC}) and the distance from the midplane ($|Z|$), is presented in Figure 8. For each bin, the mean [Fe/H] is derived. Figure 8 shows several obvious features:

(1) A gradient in both the radial and vertical direction is evident, especially near the solar circle;
(2) By the midplane, the radial gradient near the solar circle is steeper than that in the outer disk (see Sect. 3.2);
(3) The radial gradient flattens as one moves away from the midplane (see Sect. 3.2);
(4) The vertical gradient near the solar circle is steeper than that at large R_{GC} (see Sect. 3.3).

To describe those features of the spatial metallicity distribution in a quantitative manner, we measure the radial and vertical gradients separately for the different regions of the disk in the following subsections.

3.2 Radial Metallicity Gradients

The radial and vertical gradients, Δ[Fe/H]$/\Delta R_{GC}$ and Δ[Fe/H]$/\Delta Z$, are generally correlated with each other. Fortunately, with a large, contiguous disk volume sampled by a large number of stars in hand as in the current case, it is now possible to determine the radial (vertical) gradient in a thin vertical (radial) slice (annulus), and thus quantify the variations in both directions independently.

To derive the radial gradient from our RC sample, we divide the stars into bins with constant height, $\Delta|Z| = 0.2$ kpc, except for the innermost bin with $|Z| < 0.1$ kpc and the two outermost bins with $1.9 < |Z| \leq 2.4$ kpc and $2.4 < |Z| \leq 3.0$, respectively. For each bin, a straight line is adopted to fit the mean metallicities of the individual radial annuli as a function of R_{GC}. The slope of the straight line gives the radial gradient. To ensure there are a sufficient number of stars in all radial annuli, the binsize in radial direction is allowed to vary. We require that the radial binsizes are no thinner than 0.2 kpc and each radial annulus contains no less than 50 stars.

Motivated by the previous findings that the metallicity variations in the radial direction across the entire range of the disk may not be captured by a single slope, we, inspired by Magrini et al. (2009), divide the whole disk into three parts: Region A with $3 \leq R_{GC} \leq 6$ kpc, Region B with $6 \leq R_{GC} \leq 11.5$ kpc and Region C with $11.5 \leq R_{GC} \leq 22$ kpc. Region A is not covered by our RC sample, thus we only determine the radial gradients of Regions B and C for the aforementioned individual height bins. The results are presented in Figure 9. The figure shows that, close to the midplane ($|Z| < 1.0$ kpc), the gradients of Region C are flatter than those of Region B. For the upper disk ($|Z| \geq 1.0$ kpc), the radial gradients found for Regions B and C become comparable.
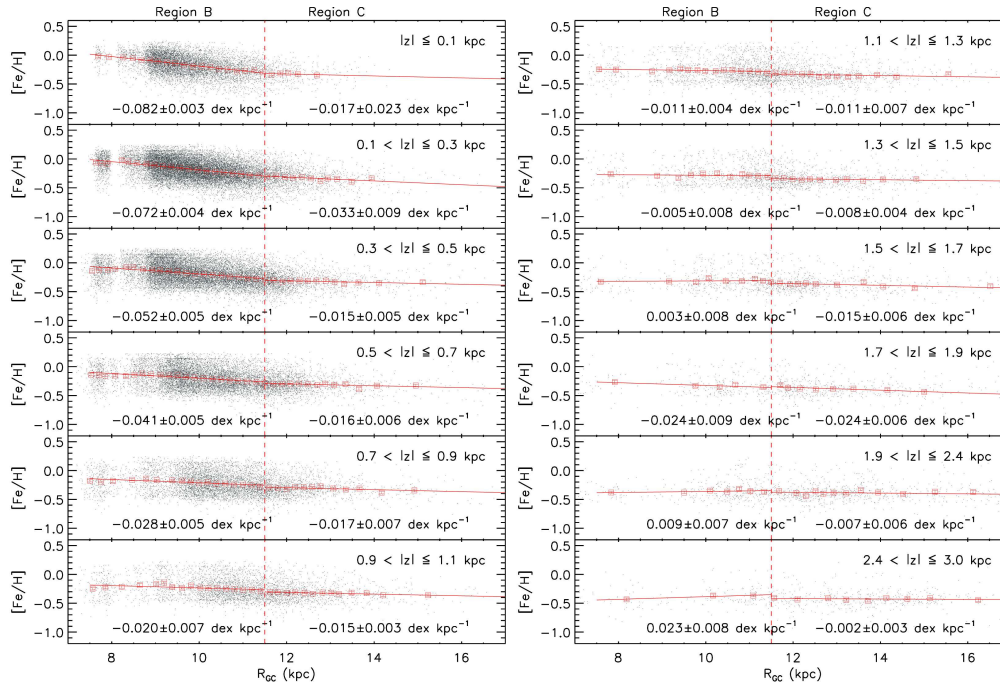
Fig. 9 Metallicity distribution as a function of R_{GC} in the individual disk height bins derived from our RC sample. The red dashed lines divide the disk into two parts: Region B near the solar circle and region C for the outer disk, as marked at the top of the two columns of the plots. Red boxes are the mean metallicities in the individual radial annuli. The metallicity gradients of Regions B and C are fitted separately, each by a straight line. The results are shown by red solid lines. The gradients and errors thus derived are also marked near the bottom of each panel.

Figure 10 plots the radial gradients measured in Regions B and C as a function of $|Z|$. For Region B, the radial gradient flattens with increasing $|Z|$. It has a negative gradient of -0.08 kpc dex^{-1} at midplane and a marginally positive gradient of 0.02 kpc dex^{-1} at ~ 2.5 kpc away from the midplane. For Region C, the gradient is essentially constant, with a value of -0.014 ± 0.008 dex kpc^{-1}.

3.3 Vertical Metallicity Gradients

To study the spatial variations of vertical gradients and also to minimize the effects of radial and vertical gradients on the determination of the vertical gradient, we divide the RC sample into annuli with width 1 kpc in the R_{GC} direction, except for the most distant annulus of $13 < R_{GC} \leq 15$ kpc. To derive the gradients, we calculate the mean metallicities of the individual height bins. The binsize in height $|Z|$ is allowed to vary but set to be no less than 0.2 kpc and each bin contains no less than 50 stars. Again, a simple straight line is used to fit the data, and the gradient is given by the slope of the fit.

The results are presented in Figure 11. The derived vertical gradients as a function of R_{GC} are presented in Figure 12. It shows that the vertical gradient flattens with increasing R_{GC}. To better understand the spatial variations of the vertical gradient, especially if there is any difference between the thin and thick disks, we further calculate the vertical gradients for the lower ($|Z| \leq 1$ kpc) and upper disk ($1 < |Z| \leq 3$ kpc) separately. The separation is chosen to be 1 kpc, where the transition
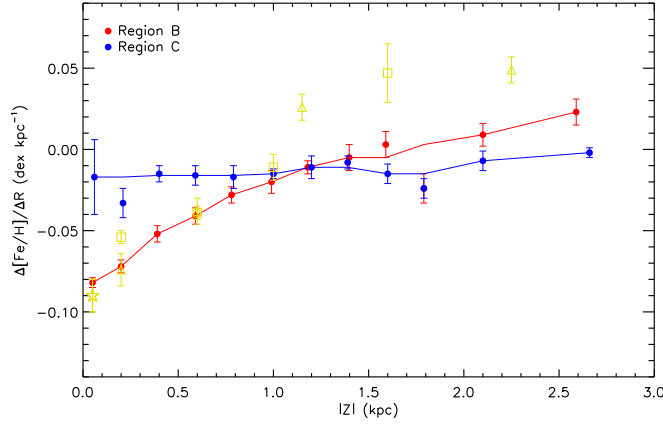
Fig. 10 Radial gradients, $\Delta[\mathrm{Fe/H}]/\Delta R_{\mathrm{GC}}$, as a function of $|Z|$ yielded by the RC sample for disk Regions B (*red dots*) and C (*blue dots*). The lines connecting the dots have been smoothed over three adjacent points. The symbols in gold represent measurements from the literature, all derived from tracers near the solar circle (i.e. Region B in this study). The star is the measurement by B14 using APOGEE RC stars, triangles the measurements by Anders et al. (2014) using APOGEE giants and boxes the measurements by Boeche et al. (2014) using RAVE RC stars.

zone is located between the thin and thick disks given their scale heights (300 pc for the thin disk and 900 pc for the thick disk; Jurić et al. 2008). As Figure 12 shows, we find that the vertical gradient of the lower disk flattens more quickly than that of the upper disk. At $R_{\mathrm{GC}} > 10.5$ kpc, the vertical gradients of the lower disk diminish to zero and even become positive, while those of the upper disk remain negative and only change slowly with R_{GC}.

4 DISCUSSIONS

The LSS-GAC DR2 RC sample presented here allows us to investigate the radial and vertical gradients over a large volume of the Galactic disk, especially its outer region. In the following subsections, we will compare our results to previous determinations and discuss their implications for Galactic disk formation and evolution.

4.1 Radial Metallicity Gradients

The gradients near the solar circle (i.e. Region B) are well determined in the current study given the large number of RC stars with accurate distances assembled here. Near the midplane ($|Z| \le 0.1$ kpc), the radial gradient measured from our RC sample has a value of 0.082 ± 0.003 dex kpc^{-1}, which is in excellent agreement with the result of 0.09 ± 0.01 dex kpc^{-1} obtained by B14, also using RC stars near the midplane ($|Z| \le 0.05$ kpc) with a similar coverage of R_{GC}. Our results show that the radial gradient flattens with increasing disk height $|Z|$. A similar trend has been found by a number of recent studies (e.g. Cheng et al. 2012; Anders et al. 2014; Boeche et al. 2014; Hayden et al. 2014).

In Figure 10 we have also overplotted the radial gradients measured at different heights $|Z|$ by Anders et al. (2014) using APOGEE red giants and by Boeche et al. (2014) using RAVE RC stars. Their measurements are generally in good agreement with our results. If one assumes that thin disk stars are concentrated more closely near the midplane than thick disk stars, the trend in variations of radial gradient with $|Z|$ may suggest that the thin disk has a negative radial metallicity gradient
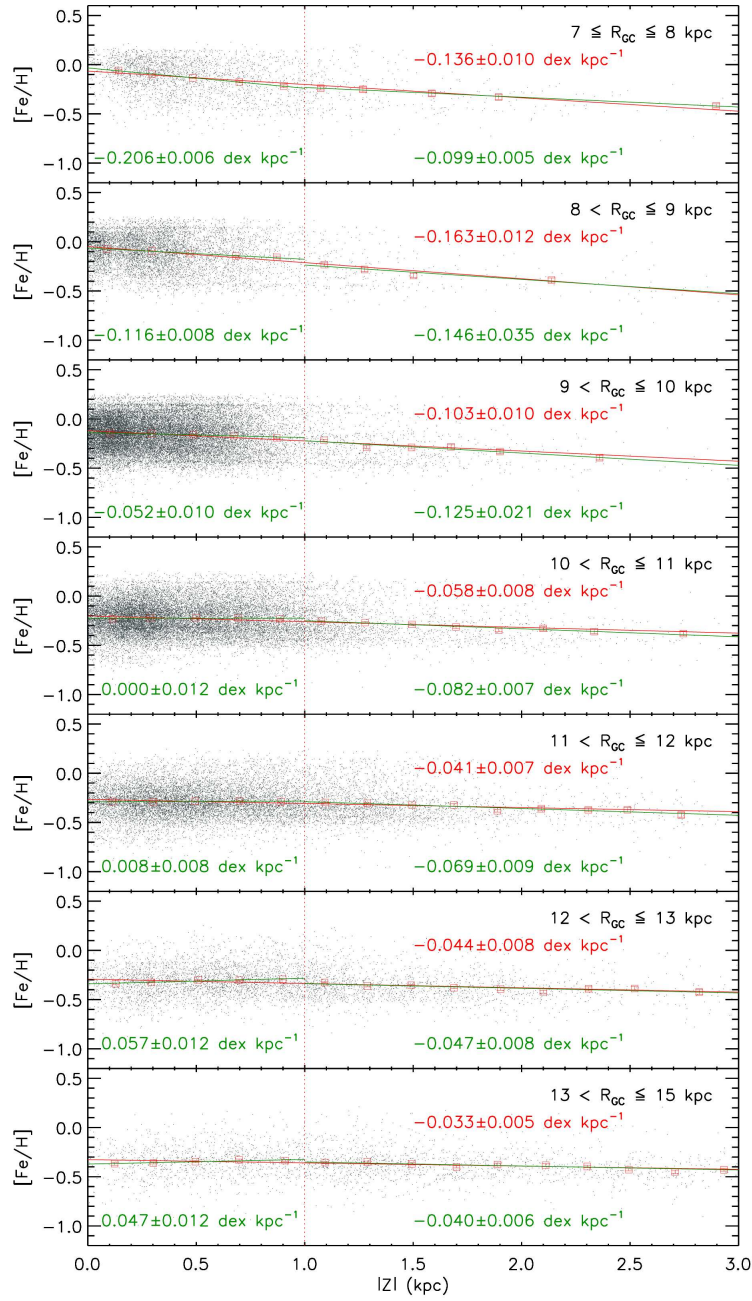
Fig. 11 Distributions of metallicities, plotted as a function of $|Z|$, deduced for the individual annuli of R_{GC} from the RC sample. The red dashed lines divide the disk into two regimes: the lower ($|Z| \leq 1$ kpc) and upper ($|Z| > 1$ kpc) disk. Red boxes show the mean metallicities in the individual vertical bins. The linear fits to the data from the lower and upper disks are shown by green lines, while those for the whole disk height are plotted in red. The gradients yielded by the fits are also marked in each plot, with the color indicating the fit.
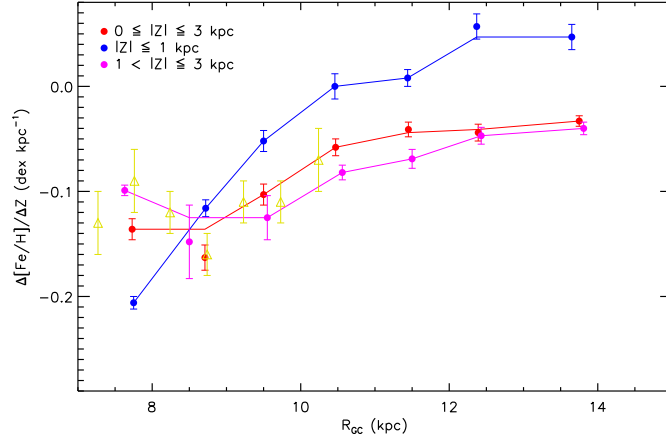
Fig. 12 Vertical gradients, $\Delta[Fe/H]/\Delta Z$, plotted as a function of R_{GC}, deduced for different ranges of disk height $|Z|$ (red: $|Z| \leq 3\,kpc$; blue: $|Z| \leq 1\,kpc$; and magenta: $1 < |Z| \leq 3\,kpc$). The lines connecting the data have been smoothed over three adjacent points. The gold triangles are measurements from Carrell et al. (2012) using SEGUE F/G/K dwarfs with $1 \leq |Z| \leq 3\,kpc$.

while the thick disk has no radial metallicity gradient. In addition, as Figure 9 shows, the data points in Region B are in general well described by a straight line with a single slope, while the mean metallicities at the inner radial annuli ($\leq 8\,kpc$) show some deviations from this slope and tend to exhibit a flatter slope even for height bins close to the midplane. Similar results have also been found recently by Hayden et al. (2014) using APOGEE red giants as tracers. This flattening of the gradient in the inner region is possibly caused by the existence of a central bar that mixes stars from different populations, as suggested by Hayden et al. (2014).

For the outer disk (i.e. Region C), as described earlier, the previous studies are not conclusive with regard to whether the gradient is flatter near the solar circle owing to the poor sampling of the available data. In the current study, with a large number of RC stars sampling the outer disk, we are able to confirm that the metallicities in the outer Region C are essentially constant, and the gradients derived are indeed less steep than those found for the solar circle. The different trends in radial gradients as a function of $|Z|$ between Region B and C, as shown in Figure 10, may suggest that these two parts of the disk may have quite different evolutionary paths, resulting from, for example, infalling gas enriched in the halo (e.g. Chiappini et al. 2001), the presence of non-axisymmetric structures (e.g. a central bar, long-lived spiral arms; e.g. Scarano & Lépine 2013), or a merger event in the outer disk (e.g. Yong et al. 2005).

4.2 Vertical Metallicity Gradients

The vertical gradients are poorly determined in previous studies. Most of those studies find a steep gradient near the solar circle, for example, -0.23 dex kpc^{-1} by Bartašiūtė et al. (2003), -0.30 dex kpc^{-1} by Chen et al. (2003) and -0.29 dex kpc^{-1} by Marsakov & Borkova (2006). Those values are all slightly steeper than our result near the solar circle. The discrepancies are possibly caused by the fact that the tracers used by those earlier studies cover a wide range of R_{GC} and the vertical gradients are deduced without binning the data in R_{RG}. Thus the values derived may be affected by the presence of a radial gradient that we have discussed in Section 3.2. The different age distributions of tracers used in different studies could also be responsible for the discrepancies. For the same R_{GC} or $|Z|$ range, our results are in excellent agreement with the previous studies. As

Figure 12 shows, the vertical gradients derived using different R_{GC} for the upper disk from our RC sample are comparable to the measurements by Carrell et al. (2012) using SEGUE F/G/K dwarfs with heights $1 \leq |Z| \leq 3\,\mathrm{kpc}$.

In the current study, we find for the first time that the vertical gradients of the lower disk ($0 < |Z| < 1\,\mathrm{kpc}$) flatten with increasing R_{GC} more quickly than those of the upper disk ($1 < |Z| < 3\,\mathrm{kpc}$). This result should provide important constraints on the formation scenarios of the thin and thick disks.

5 CONCLUSIONS

With improved $\log g$ measurements obtained with a KPCA method trained by accurate asteroseismic data from the LAMOST – *Kepler* fields, we have assembled hitherto the largest clean sample of RC stars, selected from the LSS-GAC DR2. The sample contains over 70 000 objects of intermediate ages, with a typical distance uncertainty of $5-10\,\%$. The sample stars cover a significant disk volume of projected Galactocentric radii $7 \leq R_{\mathrm{GC}} \leq 14\,\mathrm{kpc}$ and heights from the Galactic midplane $0 \leq |Z| \leq 3\,\mathrm{kpc}$. With this RC sample, we have measured the radial and vertical metallicity gradients and studied their spatial variations. The main conclusions of the current study are as follows:

(1) Both the radial and vertical gradients are negative across much of the disk probed. The gradients also show significant spatial variations;
(2) Near the solar circle ($7 \leq R_{\mathrm{GC}} \leq 11.5\,\mathrm{kpc}$), the radial gradients flatten as one moves away from the Galactic plane;
(3) In the outer disk ($11.5 \leq R_{\mathrm{GC}} \leq 14\,\mathrm{kpc}$), the radial metallicity gradients do not show clear variations with $|Z|$, and have an essentially constant value of $-0.014\,\mathrm{dex\,kpc^{-1}}$ that is much shallower than near the solar circle. This suggests that the outer disk may have a very different evolutionary path;
(4) The vertical gradients also show significant spatial variations, flattening with increasing R_{GC}. More interestingly, for the first time, we find the vertical gradients of the lower disk ($0 < |Z| \leq 1\,\mathrm{kpc}$) flatten with R_{GC} more quickly than those of the upper disk ($1 < |Z| \leq 3\,\mathrm{kpc}$).

For the moment, the chemical or chemo-dynamical models cannot fully predict the spatial variations of metallicity gradients found in the current work. Our results suggest that processes such as radial migration, non-axisymmetric perturbation, and galaxy mergers may have played a significant role in shaping the Galactic disk(s). The LSS-GAC survey is an ongoing project and will last until 2017. With more observations becoming available, the size and spatial coverage of our sample will continue to expand. In addition, more information, especially the [α/Fe] ratios, will become available with a newer version of LSP3. As the survey progresses, the LSS-GAC survey will no doubt continue to provide further, stronger constraints on the chemical enrichment history of the Galactic disk(s), and shed light on the formation and evolution of the Galaxy.

Appendix A:

The number of PCs adopted in our current KPCA model, i.e. $N_{\mathrm{PC}} = 25$, is a tradeoff between the following two considerations. Firstly, a sufficient number of PCs is required to construct a tight relation between asteroseismic $\log g$ and LAMOST blue-arm spectral features.

As Figure A.1 shows, when N_{PC} is small, the fit of the residuals shows large systematics. When $N_{\mathrm{PC}} \geq 25$, the fit of the residuals no longer shows an obvious trend as the atmospheric parameters vary and the standard deviations of the fit residuals slowly decrease with increasing N_{PC}. On the other hand, a value of N_{PC} that is too large will lead to biased estimates of $\log g$ under low values of S/N for the spectra.

As Figure A.2 shows, the systematics become quite significant for values of spectral S/N smaller than 20 if $N_{\mathrm{PC}} \geq 30$. Hence, in the current work we have adopted $N_{\mathrm{PC}} = 25$ for the KPCA model in constructing the relation between asteroseismic $\log g$ and LAMOST blue-arm spectral features.
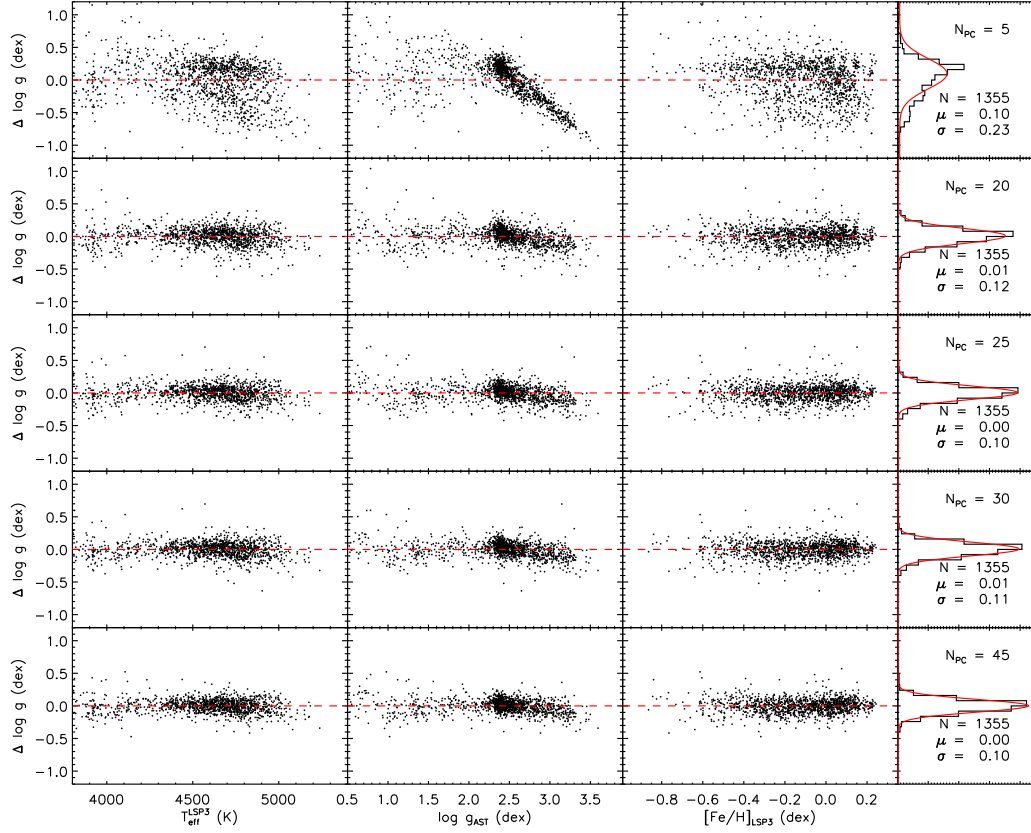

Fig. A.1 Distributions of values of residual, $\log g_{\mathrm{KPCA}} - \log g_{\mathrm{AST}}$, for the training sample, as a function of LSP3 T_{eff} and [Fe/H] and of asteroseismic $\log g$ for different N_{PC} assumed. The last panel in each subplot shows a histogram distribution of the residuals (*black line*). Also overplotted in red is a Gaussian fit to the distribution. The mean and dispersion of the fit, as well as the number of stars used, are marked.
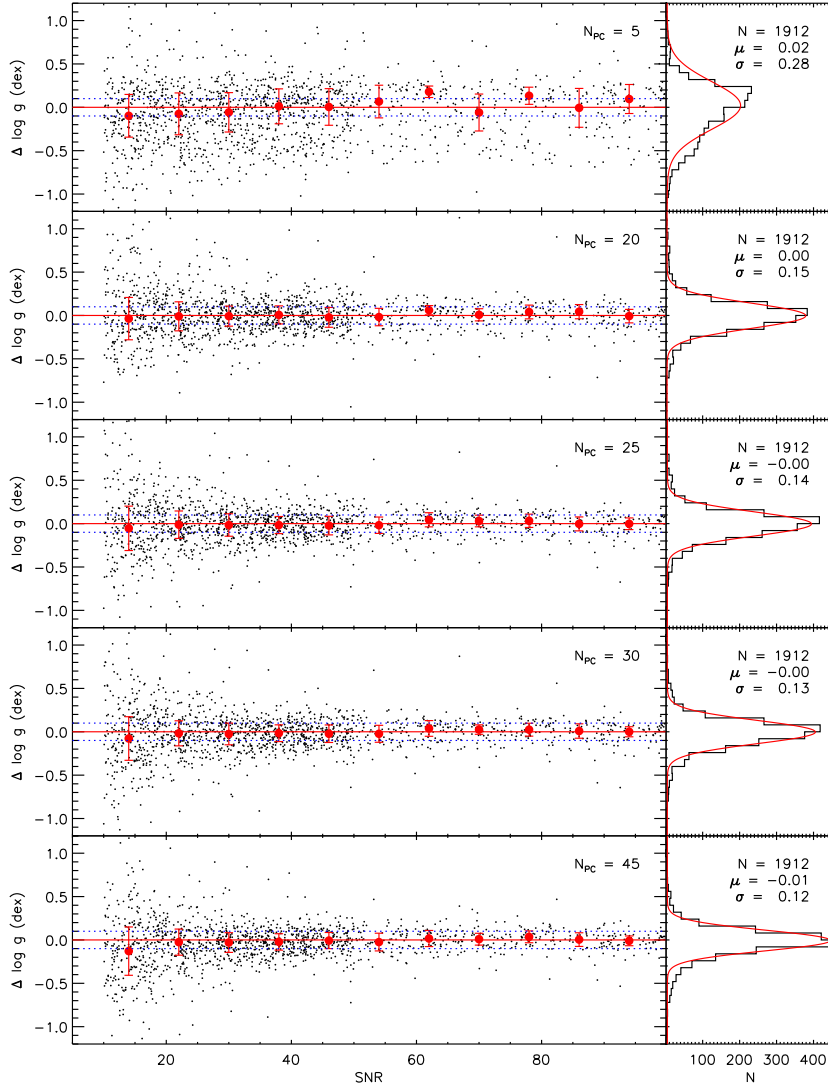
Fig. A.2 Differences in KPCA $\log g$ estimates and asteroseismic values for the control sample, plotted as a function of spectral S/N (4650 Å) for different N_{PC} assumed. The blue dashed lines indicate the differences $\Delta \log g = \pm 0.1$ dex. The means and standard deviations of the differences in the individual S/N (4650 Å) bins (binsize = 8) are oveplotted with dots and error bars, respectively.

References

Ahn, C. P., Alexandroff, R., Allende Prieto, C., et al. 2014, ApJS, 211, 17

Allende Prieto, C., Beers, T. C., Wilhelm, R., et al. 2006, ApJ, 636, 804

Allende Prieto, C., Majewski, S. R., Schiavon, R., et al. 2008, Astronomische Nachrichten, 329, 1018

Anders, F., Chiappini, C., Santiago, B. X., et al. 2014, A&A, 564, A115

Andrievsky, S. M., Kovtyukh, V. V., Luck, R. E., et al. 2002a, A&A, 381, 32

Andrievsky, S. M., Bersier, D., Kovtyukh, V. V., et al. 2002b, A&A, 384, 140

Andrievsky, S. M., Kovtyukh, V. V., Luck, R. E., et al. 2002c, A&A, 392, 491

Andrievsky, S. M., Luck, R. E., Martin, P., & Lépine, J. R. D. 2004, A&A, 413, 159

Balser, D. S., Rood, R. T., Bania, T. M., & Anderson, L. D. 2011, ApJ, 738, 27

Bartašiūtė, S., Aslan, Z., Boyle, R. P., et al. 2003, Baltic Astronomy, 12, 539

Belkacem, K., Goupil, M. J., Dupret, M. A., et al. 2011, A&A, 530, A142

Bertelli, G., Bressan, A., Chiosi, C., Fagotto, F., & Nasi, E. 1994, A&AS, 106, 275

Bienaymé, O., Famaey, B., Siebert, A., et al. 2014, A&A, 571, A92

Bilir, S., Karaali, S., Ak, S., et al. 2012, MNRAS, 421, 3362

Boeche, C., Siebert, A., Piffl, T., et al. 2013, A&A, 559, A59

Boeche, C., Siebert, A., Piffl, T., et al. 2014, A&A, 568, A71

Borucki, W. J., Koch, D., Basri, G., et al. 2010, Science, 327, 977

Bovy, J., Nidever, D. L., Rix, H.-W., et al. 2014, ApJ, 790, 127

Bressan, A., Marigo, P., Girardi, L., et al. 2012, MNRAS, 427, 127

Brown, T. M., Gilliland, R. L., Noyes, R. W., & Ramsey, L. W. 1991, ApJ, 368, 599

Cannon, R. D. 1970, MNRAS, 150, 111

Carraro, G., Geisler, D., Villanova, S., Frinchaboy, P. M., & Majewski, S. R. 2007, A&A, 476, 217

Carrell, K., Chen, Y., & Zhao, G. 2012, AJ, 144, 185

Carrera, R., & Pancino, E. 2011, A&A, 535, A30

Casagrande, L., Schönrich, R., Asplund, M., et al. 2011, A&A, 530, A138

Chabrier, G. 2001, ApJ, 554, 1274

Chen, L., Hou, J. L., & Wang, J. J. 2003, AJ, 125, 1397

Chen, Y. Q., Zhao, G., Carrell, K., & Zhao, J. K. 2011, AJ, 142, 184

Cheng, J. Y., Rockosi, C. M., Morrison, H. L., et al. 2012, ApJ, 746, 149

Chiappini, C., Matteucci, F., & Gratton, R. 1997, ApJ, 477, 765

Chiappini, C., Matteucci, F., & Romano, D. 2001, ApJ, 554, 1044

Costa, R. D. D., Uchida, M. M. M., & Maciel, W. J. 2004, A&A, 423, 199

Creevey, O. L., Thévenin, F., Basu, S., et al. 2013, MNRAS, 431, 2419

Cui, X.-Q., Zhao, Y.-H., Chu, Y.-Q., et al. 2012, RAA (Research in Astronomy and Astrophysics), 12, 1197

Daflon, S., & Cunha, K. 2004, ApJ, 617, 1115

Daflon, S., Cunha, K., de la Reza, R., Holtzman, J., & Chiappini, C. 2009, AJ, 138, 1577

De Cat, P., Fu, J., Yang, X., et al. 2014, arXiv:1411.0913

Deharveng, L., Peña, M., Caplan, J., & Costero, R. 2000, MNRAS, 311, 329

Deng, L.-C., Newberg, H. J., Liu, C., et al. 2012, RAA (Research in Astronomy and Astrophysics), 12, 735

Epstein, C. R., Elsworth, Y. P., Johnson, J. A., et al. 2014, ApJ, 785, L28

ESA, ed. 1997, ESA Special Publication, 1200, The HIPPARCOS and TYCHO catalogues. Astrometric and photometric star catalogues derived from the ESA HIPPARCOS Space Astrometry Mission

Friel, E. D., Janes, K. A., Tavarez, M., et al. 2002, AJ, 124, 2693

Friel, E. D., Jacobson, H. R., & Pilachowski, C. A. 2010, AJ, 139, 1942

Frinchaboy, P. M., Thompson, B., Jackson, K. M., et al. 2013, ApJ, 777, L1

Fu, J., Hou, J. L., Yin, J., & Chang, R. X. 2009, ApJ, 696, 668

Genovali, K., Lemasle, B., Bono, G., et al. 2013, A&A, 554, A132

Genovali, K., Lemasle, B., Bono, G., et al. 2014, A&A, 566, A37

Gummersbach, C. A., Kaufer, A., Schaefer, D. R., Szeifert, T., & Wolf, B. 1998, A&A, 338, 881

Hayden, M. R., Holtzman, J. A., Bovy, J., et al. 2014, AJ, 147, 116

Henry, R. B. C., Kwitter, K. B., & Balick, B. 2004, AJ, 127, 2284

Henry, R. B. C., Kwitter, K. B., Jaskot, A. E., et al. 2010, ApJ, 724, 748

Hou, J. L., Prantzos, N., & Boissier, S. 2000, A&A, 362, 921

Huber, D., Silva Aguirre, V., Matthews, J. M., et al. 2014, ApJS, 211, 2

Jacobson, H. R., Friel, E. D., & Pilachowski, C. A. 2008, AJ, 135, 2341

Jacobson, H. R., Friel, E. D., & Pilachowski, C. A. 2009, AJ, 137, 4753

Jacobson, H. R., Friel, E. D., & Pilachowski, C. A. 2011a, AJ, 141, 58

Jacobson, H. R., Pilachowski, C. A., & Friel, E. D. 2011b, AJ, 142, 59

Jurić, M., Ivezić, Ž., Brooks, A., et al. 2008, ApJ, 673, 864

Katz, D., Soubiran, C., Cayrel, R., et al. 2011, A&A, 525, A90

Kordopatis, G., Recio-Blanco, A., de Laverny, P., et al. 2011, A&A, 535, A107

Kovtyukh, V. V., Wallerstein, G., & Andrievsky, S. M. 2005, PASP, 117, 1173

Kubryk, M., Prantzos, N., & Athanassoula, E. 2013, MNRAS, 436, 1479

Laney, C. D., Joner, M. D., & Pietrzyński, G. 2012, MNRAS, 419, 1637

Larson, R. B. 1976, MNRAS, 176, 31

Lemasle, B., François, P., Bono, G., et al. 2007, A&A, 467, 283

Lemasle, B., François, P., Piersimoni, A., et al. 2008, A&A, 490, 613

Lemasle, B., François, P., Genovali, K., et al. 2013, A&A, 558, A31

Liu, C., Fang, M., Wu, Y., et al. 2015, ApJ, 807, 4

Liu, X.-W., Yuan, H.-B., Huo, Z.-Y., et al. 2014, in IAU Symposium, 298, eds. S. Feltzing, G. Zhao, N. A.
    Walton, & P. Whitelock, 310

Liu, X. W., Zhao, G., & Hou, J. L. 2015, RAA (Research in Astronomy and Astrophysics), 15, 1089

Loebman, S. R., Roškar, R., Debattista, V. P., et al. 2011, ApJ, 737, 8

Luck, R. E., Gieren, W. P., Andrievsky, S. M., et al. 2003, A&A, 401, 939

Luck, R. E., Kovtyukh, V. V., & Andrievsky, S. M. 2006, AJ, 132, 902

Luck, R. E., Andrievsky, S. M., Kovtyukh, V. V., Gieren, W., & Graczyk, D. 2011, AJ, 142, 51

Luck, R. E., & Lambert, D. L. 2011, AJ, 142, 136

Luo, A.-L., Zhao, Y.-H., Zhao, G., et al. 2015, RAA (Research in Astronomy and Astrophysics), 15, 1095

Maciel, W. J., Lago, L. G., & Costa, R. D. D. 2005, A&A, 433, 127

Magrini, L., Sestito, P., Randich, S., & Galli, D. 2009, A&A, 494, 95

Magrini, L., Randich, S., Zoccali, M., et al. 2010, A&A, 523, A11

Marsakov, V. A., & Borkova, T. V. 2006, Astronomy Letters, 32, 376

Martin, R. P., Andrievsky, S. M., Kovtyukh, V. V., et al. 2015, MNRAS, 449, 4071

Matteucci, F., & Francois, P. 1989, MNRAS, 239, 885

Minchev, I., Chiappini, C., & Martig, M. 2013, A&A, 558, A9

Mollá, M., Ferrini, F., & Díaz, A. I. 1997, ApJ, 475, 519

Mollá, M., & Díaz, A. I. 2005, MNRAS, 358, 521

Paczyński, B., & Stanek, K. Z. 1998, ApJ, 494, L219

Pedicelli, S., Bono, G., Lemasle, B., et al. 2009, A&A, 504, 81

Pedicelli, S., Lemasle, B., Groenewegen, M., et al. 2010, A&A, 518, A11

Perinotto, M., & Morbidelli, L. 2006, MNRAS, 372, 45

Pinsonneault, M. H., Elsworth, Y., Epstein, C., et al. 2014, ApJS, 215, 19

Portinari, L., & Chiosi, C. 1999, A&A, 350, 827

Prantzos, N., & Boissier, S. 2000, MNRAS, 313, 338

Puzeras, E., Tautvaišienė, G., Cohen, J. G., et al. 2010, MNRAS, 408, 1225

Quireza, C., Rood, R. T., Bania, T. M., Balser, D. S., & Maciel, W. J. 2006, ApJ, 653, 1226

Re Fiorentin, P., Bailer-Jones, C. A. L., Lee, Y. S., et al. 2007, A&A, 467, 1373

Rees, D. E., López Ariste, A., Thatcher, J., & Semel, M. 2000, A&A, 355, 759

Roeser, S., Demleitner, M., & Schilbach, E. 2010, AJ, 139, 2440

Rolleston, W. R. J., Smartt, S. J., Dufton, P. L., & Ryans, R. S. I. 2000, A&A, 363, 537

Rudolph, A. L., Fich, M., Bell, G. R., et al. 2006, ApJS, 162, 346

Scarano, S., & Lépine, J. R. D. 2013, MNRAS, 428, 625

Schlesinger, K. J., Johnson, J. A., Rockosi, C. M., et al. 2012, ApJ, 761, 160

Schlesinger, K. J., Johnson, J. A., Rockosi, C. M., et al. 2014, ApJ, 791, 112

Schölkopf, B., Smola, A., & Müller, K.-R. 1998, Neural computation, 10, 1299

Schönrich, R., & Binney, J. 2009, MNRAS, 396, 203

Siebert, A., Famaey, B., Minchev, I., et al. 2011, MNRAS, 412, 2026

Singh, H. P., Gulati, R. K., & Gupta, R. 1998, MNRAS, 295, 312

Skrutskie, M. F., Cutri, R. M., Stiening, R., et al. 2006, AJ, 131, 1163

Smartt, S. J., & Rolleston, W. R. J. 1997, ApJ, 481, L47

Stanek, K. Z., & Garnavich, P. M. 1998, ApJ, 503, L131

Stanghellini, L., Guerrero, M. A., Cunha, K., Manchado, A., & Villaver, E. 2006, ApJ, 651, 898

Stanghellini, L., & Haywood, M. 2010, ApJ, 714, 1096

Steinmetz, M., Zwitter, T., Siebert, A., et al. 2006, AJ, 132, 1645

Stello, D., Huber, D., Bedding, T. R., et al. 2013, ApJ, 765, L41

Tosi, M. 1988, A&A, 197, 33

Vilchez, J. M., & Esteban, C. 1996, MNRAS, 280, 720

Williams, M. E. K., Steinmetz, M., Binney, J., et al. 2013, MNRAS, 436, 101

Wu, Y., Luo, A.-L., Li, H.-N., et al. 2011, RAA (Research in Astronomy and Astrophysics), 11, 924

Xiang, M. S., Liu, X. W., Yuan, H. B., et al. 2015a, MNRAS, 448, 90

Xiang, M. S., Liu, X. W., Yuan, H. B., et al. 2015b, MNRAS, 448, 822

Xiang, M. S., Liu, X. W., Yuan, H. B., et al. 2015c, RAA (Research in Astronomy and Astrophysics), 15, 1209

Yanny, B., Rockosi, C., Newberg, H. J., et al. 2009, AJ, 137, 4377

Yong, D., Carney, B. W., & Teixera de Almeida, M. L. 2005, AJ, 130, 597

Yong, D., Carney, B. W., Teixera de Almeida, M. L., & Pohl, B. L. 2006, AJ, 131, 2256

Yong, D., Carney, B. W., & Friel, E. D. 2012, AJ, 144, 95

York, D. G., Adelman, J., Anderson, Jr., J. E., et al. 2000, AJ, 120, 1579

Yuan, H.-B., Liu, X.-W., Huo, Z.-Y., et al. 2015, MNRAS, 448, 855

Zacharias, N., Finch, C. T., Girard, T. M., et al. 2013, AJ, 145, 44